IRON-RICH EJECTA DISTRIBUTION FROM LUNAR BASIN IMPACTS: RELATIONSHIP TO LUNAR CRUSTAL MAGNETISM.

R. I. Citron[1,2], L. L. Hood[3] and S. T. Stewart[4], [1]Earth, Atmospheric and Planetary Sciences, Massachusetts Institute of Technology, Cambridge, MA 02139 (rcitron@mit.edu), [2]NASA Goddard Spaceflight Center, Greenbelt, MD, [3]Lunar and Planetary Laboratory, University of Arizona, Tuscon, AZ, [4]Department of Earth and Planetary Sciences, University of California, Davis, CA.

Introduction: The origin of lunar crustal anomalies remains enigmatic. While crustal magnetic signatures are detected over multiple portions of the crust, the crust that formed from the lunar magma ocean had a low abundance of magnetic phases and typical lunar crustal materials do not retain strong magnetization. This motivates the hypothesis that the carriers of magnetic remanence in the crust (i.e., metallic iron) may be largely sourced from iron-rich impactor material after crust formation [1]. Specifically, metallic iron in impacting bodies could be the strongest carrier of magnetism in the lunar crust.

Improved mapping of the lunar magnetic field has shown that many crustal anomalies are oriented radial to the Imbrium basin and others may be oriented radial to the Orientale basin [2]. This adds to previous evidence for concentrations of anomalies antipodal to young large basins [3]. While simulations show that lunar basin-forming impacts can deposit ejecta antipodal to the impact site [4, 5], the full radial orientation and concentration of iron-enriched ejecta at the antipode remain unexplored for a range of impact parameters.

Here, using a suite of 3D impact hydrocode simulations, we explore the range of model parameters (impactor size, iron content, velocity, and angle) that results in iron-enriched ejecta deposited radially and antipodal to lunar impact basins.

Lunar magnetic anomalies: A series of lunar magnetic anomalies on the near side have been found to lie along great circle paths oriented radial to the Imbrium basin [2]. This includes named anomalies such as Reiner Gamma, Hartwig, Descartes, Abel, and Airy. Groupings of anomalies may also be oriented radial to and antipodal to the Orientale, Serenitatis, Crisium, and Schrodinger basins [2, 6]. The concentration and distribution of magnetic anomalies relative to lunar impact basins has been proposed to be related to iron-rich impactor material ejected during basin forming impacts [1, 4, 5]. In particular, material from the projectile could become magnetized after ejection as it cools from its expected post-impact molten state.

Numerical studies show that ejecta from basin forming impacts can concentrate ejecta sourced from the projectile antipodal to the impact site [4, 5]. While more ejecta is deposited closer to the impact basin, the convergence of radially ejected material at the antipode can concentrate material there. Recent simulations have concentrated on 100 km diameter projectiles impacting a planar surface [5]. Here, we test a range of impact parameters and projectile types for collisions onto a spherical body.

Methods: We modeled 3D lunar basin-forming impacts using the numerical shock hydrocode CTH [7]. We used an updated version of the ANEOS equation of state with new parameters for pyrolite and Fe-Si iron alloy to model the planetary mantle and core, respectively [8, 9]. Improvements to the ANEOS equation of state used in this work provide more accurate estimates of material vaporization during the impact, which could lead to differences compared to previous work. Crust was modeled with updated ANEOS parameters for anorthosite. Material strength for the mantle and crust was modeled using a strain-rate dependent damage accumulation model based on [10], which has been updated to include dynamic fault weakening [11, 12]. Simulations were conducted in 3D with self gravity. We conducted a set of simulations varying impactor diameter (D = 50, 100, 175, or 250 km), impact velocity (10,

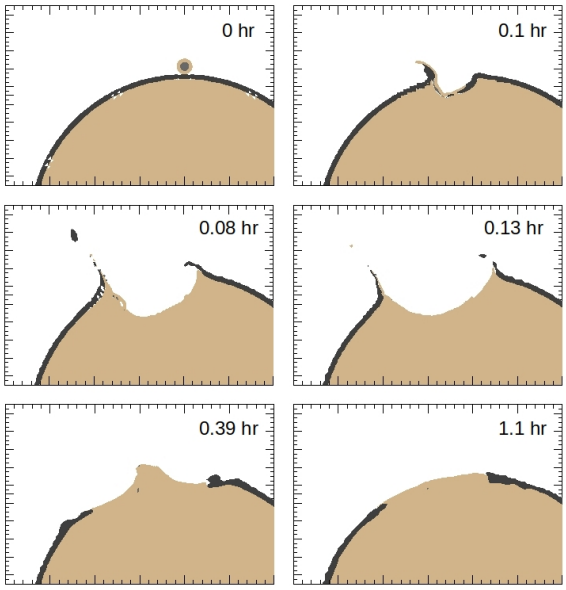

Figure 1: Example simulation of a D=175 km differentiated projectile impacting the Moon at v_{imp}=20 km/s and θ=45°. The iron core is shown in light grey.

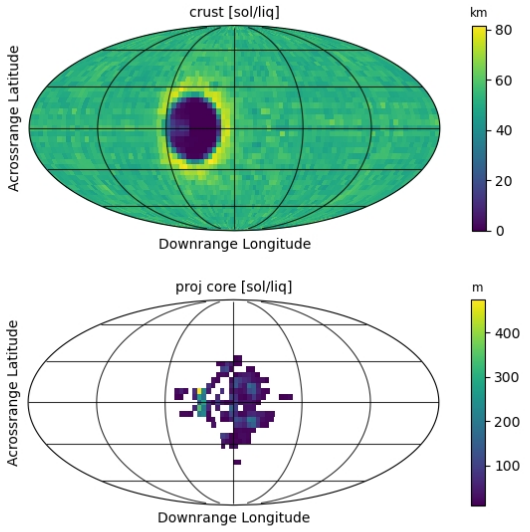

Figure 2: Post-impact crustal thickness distribution (top) and distribution of projectile iron (bottom) for a *differentiated* D=175 km impact at 20 km/s and θ=45°.

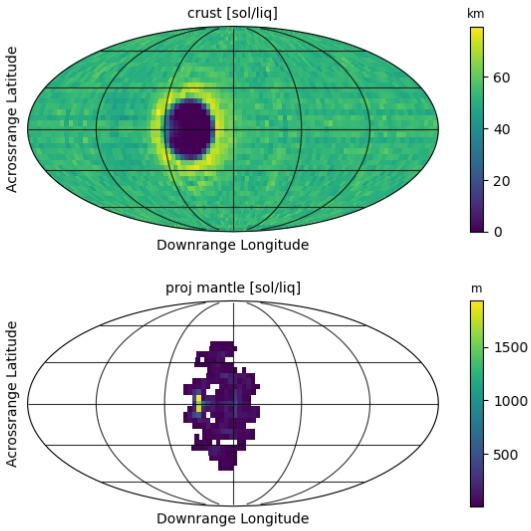

Figure 3: Post-impact crustal thickness distribution (top) and distribution of projectile mantle (bottom) for an *undifferentiated* D=175 km impact at 20 km/s and θ=45°.

20, or 30 km/s), and impact angle (0, 30, 45, or 60°), and tested both differentiated and undifferentiated projectiles. An example simulation is shown in Fig. 1.

Results and discussion: Preliminary results for a D=175km diameter impactor are shown for a differentiated projectile (Fig. 2) and undifferentiated projectile (Fig. 3). For the differentiated case, projectile iron is tracked and the thickness at the end of the simulation is computed over a 4 degree-per-pixel grid. For the undifferentiated projectile case, the thickness of projectile mantle is computed, and it is assumed that the iron-rich projectile mantle material could retain magnetization.

For both the differentiated and undifferentiated projectile cases, impactor ejecta material is concentrated close to the impact basin. While significant portions of projectile material are deposited downrange, extending radially away from the downrange rim of the impact basin, projectile material is not deposited at the antipode. However, we note that the thickness of material plotted is only for ejecta in a liquid and solid state post-impact; vapor and supercritical fluid ejecta travels further and could rain out at greater distances. In order to ensure the lack of more distant ejecta is not due to inaccuracies in the code tracking material traveling such distances with accurate phase state, we are currently updating our analysis to include a computation of the ballistic trajectories of ejected material to compare with the full distribution of material computed post-impact.

While our initial analysis shows only radial ejecta concentrations and a lack of antipodal ejecta, additional simulations at varying impact parameters may result in varying ejecta distributions. In particular, more oblique impacts can result in a higher portion of material deposited downrange and closer to the antipode [5]. Ongoing work to compare the distribution of ejecta from direct simulation output to the inferred distribution from ballistic trajectories will determine the extent to which the post-impact vapor plume affects ejecta trajectories and emplacement.

Acknowledgements: This work is supported by NASA LDAP Grant 80NSSC21K1478.

References: [1] Wieczorek M. A. et al. (2012) *Science*, *335*, 1212–1215. [2] Hood L. L. et al. (2021) *Journal of Geophysical Research: Planets*, *126*. [3] Mitchell D. et al. (2008) *Icarus*, *194*, 401–409. [4] Hood L. L. and Artemieva N. A. (2008) *Icarus*, *193*, 485–502. [5] Wakita S. et al. (2021) *Nature Communications*, *12*, 1–7. [6] Hood L. L. et al. (2022) *Geophysical Research Letters*, *49*, e2022GL100557. [7] McGlaun J. M. et al. (1990) *International Journal of Impact Engineering*, *10*, 351–360. [8] Kovačević T. et al. (2022) *Scientific Reports*, *12*, 1–11. [9] Stewart S. T., Equation of State Model Fe85Si15-ANEOS: Development and documentation (Version SLVTv0.2G1) (2020), *Zenodo*, 10.5281/zenodo.3866550. [10] Collins G. S. et al. (2004) *Meteoritics and Planetary Science*, *39*, 217–231. [11] Senft L. E. and Stewart S. T. (2007) *Journal of Geophysical Research E: Planets*, *112*, 1–18. [12] Senft L. E. and Stewart S. T. (2009) *Earth and Planetary Science Letters*, *287*, 471–482.